

Theoretical wavelet ℓ_1 -norm from one-point PDF prediction

Vilasini Tinnaneri Sreekanth¹, Sandrine Codis¹, Alexandre Barthelemy², and Jean-Luc Starck^{1,3}

¹ Université Paris-Saclay, Université Paris Cité, CEA, CNRS, AIM, 91191, Gif-sur-Yvette, France
e-mail: vilasini.tinnaneri@sreekanth@cea.fr

² Universitäts-Sternwarte, Fakultät für Physik, Ludwig-Maximilians-Universität München, Scheinerstraße 1, 81679 München, Germany

³ Institutes of Computer Science and Astrophysics, Foundation for Research and Technology Hellas (FORTH), Greece

Received ?; accepted ?

ABSTRACT

Context. Weak gravitational lensing, resulting from the bending of light due to the presence of matter along the line of sight, is a potent tool for exploring large-scale structures, particularly in quantifying non-Gaussianities. It stands as a pivotal objective for upcoming surveys. In the realm of current and forthcoming full-sky weak-lensing surveys, the convergence maps, representing a line-of-sight integration of the matter density field up to the source redshift, facilitate field-level inference, providing an advantageous avenue for cosmological exploration. Traditional two-point statistics fall short of capturing non-Gaussianities, necessitating the use of higher-order statistics to extract this crucial information. Among the various higher-order statistics available, the wavelet ℓ_1 -norm has proven its efficiency in inferring cosmology (Ajani et al. (2021)). However, the lack of a robust theoretical framework mandates reliance on simulations, demanding substantial resources and time.

Aims. Our novel approach introduces a theoretical prediction of the wavelet ℓ_1 -norm for weak lensing convergence maps, grounded in the principles of Large-Deviation theory. This method builds upon recent work by Barthelemy et al. (2021), offering a theoretical prescription for aperture mass one-point probability density function.

Methods. We present, for the first time, a theoretical prediction of the wavelet ℓ_1 -norm for convergence maps, derived from the theoretical prediction of their one-point probability distribution. Additionally, we explore the cosmological dependence of this prediction and validate the results on simulations.

Results. A comparison of our predicted wavelet ℓ_1 -norm with simulations demonstrates a high level of accuracy in the weakly non-linear regime. Moreover, we show its ability to capture cosmological dependence, paving the way for a more robust and efficient parameter inference process.

Key words. higher order statistics – κ -PDF – ℓ_1 -norm – large deviation theory – non-gaussianities

1. Introduction

Our present comprehension of the genesis of large-scale structure (Peebles 1980) posits that it emerged through gravitational instability driven by primordial fluctuations in matter density. Realistic models detailing structure formation prescribe an initial spectrum of perturbations reflecting the primordial spectrum, characterised by small fluctuations at large scales. In an LCDM Universe, the variance of the density fluctuations, denoted by $\sigma(R)^2$, is inversely proportional to (some power of) scales so that at small scales, the variance is large and non-linear effects become important.

Hence, there are two limiting regimes: the linear regime which is characterized by $\sigma^2(R) \ll 1$, and the non-linear regime which is given by $\sigma^2(R) \gg 1$. In particular, if the primordial density fluctuations are Gaussian, then they remain Gaussian in the subsequent linear regime, and Fourier modes evolve independently. However, the coupling between different Fourier modes becomes significant and plays a pivotal role in modifying the statistical properties, manifesting as higher-order connected correlations in the non-linear regime (Bernardeau et al. 2002).

One of the powerful methods, to probe these non-linearities present in the large-scale structure (hereafter LSS) is to look at the distortions of the distant images of galaxies. Distortions happen because of gravitational lensing, which is the phenomenon in which the paths of the photons are bent due to the presence of

massive objects such as galaxies or galaxy clusters. Weak gravitational lensing denotes that, except for rare cases of strong lensing, these distortions are often subtle, requiring statistical analysis over a vast number of galaxies to detect a signal. Analyzing these distortions provides a unique opportunity to investigate the distribution of matter in the Universe and infer cosmological parameters. For a more comprehensive review of weak lensing, readers are referred to (Mandelbaum (2018); Kilbinger (2018)), and Kilbinger (2015).

In this era of precision cosmology, with past, present, and future surveys such as the Canada-France-Hawaii Telescope Lensing Survey (CFHTLenS) (Heymans et al. 2012), Hyper Suprime-Cam (HSC) (Mandelbaum & Collaboration 2017), *Euclid* (Laureijs et al. 2011), *LSST* (Ivezić et al. 2019)), to name a few, we now have access to the non-Gaussian part of cosmological signals, which are induced by the non-linear evolution of the structures on small scales. All of these experiments, consider weak gravitational lensing to be a key probe – jointly with galaxy clustering – to explore the current unanswered questions in Cosmology like the neutrino mass sum (Lesgourgues & Pastor 2012; Li et al. 2019), the nature of dark energy and dark matter (Huterer 2010), and it offers substantial constraints on standard cosmological parameters like the mean matter density, the amplitude of matter fluctuations (Troxel & Ishak 2015).

The conventional approach to infer the cosmology from the data involves the computation of the two-point statistics, which has been employed with remarkable success in the past (Munshi et al. 2008; Kilbinger 2015; Bartelmann & Maturi 2017; Hildebrandt et al. 2017) ((Euclid Collaboration et al. 2024; Loureiro et al. 2023; Ingolia et al. 2022)). However, it is not sufficient if we want to probe the non-Gaussianities present (Weinberg et al. 2013). This limitation arises from the construction of the power spectrum, which considers information solely from the norm of wave-vectors while neglecting phase information, thereby discarding a significant aspect of structural details. Consequently, there arises a necessity to complement this approach with an alternative higher-order statistic capable of effectively capturing the non-Gaussian features embedded in the structure. Higher-order statistics such as peak counts (Kruse & Schneider 1999; Liu et al. 2015a,b; Lin & Kilbinger 2015; Peel et al. 2017; Ajani et al. 2020), higher moments (Petri 2016; Peel et al. 2018; Gatti et al. 2020), Minkowski functional (Kratochvil et al. 2012; Parroni et al. 2020), three-point statistics (Takada & Jain 2004; Semboloni et al. 2011; Rizzato et al. 2019) and wavelet and scattering transform (Ajani et al. 2021; Cheng & Ménard 2021) amongst many others, can better probe the non-Gaussian structure of the Universe and provide additional constraints on the cosmological parameters. Another example was given in Ajani et al. (2021) employing the starlet ℓ_1 -norm that has the advantage of being easy to measure and was claimed to encompass even more cosmological information than the power spectrum or peak and void counts in the setting considered. The ℓ_1 -norm of a starlet, which is a type of wavelet that uses $B3$ -spline, offers an efficient multi-scale computation of all map pixels including the under-densities and over-densities distribution, partially probing similar information to peak and void counts.

The Probability Distribution Function (hereafter PDF) of the weak lensing convergence map (κ) serves as another valuable repository of cosmological information that has drawn a lot of interest in recent years, with many theoretical and numerical works including (Bernardeau & Valageas 2001; Liu & Madhavacheril 2019; Barthelemy et al. 2021). The convergence field κ represents the weighted projection of matter density fluctuations along the line of sight and its higher-order correlations offer a promising avenue for addressing challenges inherent in standard weak lensing analyses, particularly those related to degeneracies in the two-point correlation function (2PCF).

The one-point κ -PDF statistic, obtained by quantifying smoothed κ field values within predefined apertures or cells, presents a practical advantage as its measure is rather simple. This simplicity contrasts with other non-Gaussian probes used for studying the weak lensing convergence field, such as the bispectrum (which involves counting triangular configurations) or Minkowski functionals (a topological measurement). Previous research has successfully devised a precise theoretical model, grounded in large deviation theory (LDT), for both the cumulant generating function and the PDF of the lensing κ field as well as the aperture mass (Barthelemy et al. 2021). Notably, this one-point PDF could be directly linked to the wavelet coefficients at different scales (Ajani et al. 2021).

Let us emphasize that similarly to the convergence PDF, all of the above-mentioned non-Gaussian statistics, which probe deviations from Gaussian behaviour, are also commonly computed using the convergence maps. However, these convergence maps are not observed directly and are reconstructed from the reduced shear maps. The shear maps since its first detection two decades ago (Bacon et al. 2000; Kaiser et al. 2000; Waerbeke et al. 2000) have been a powerful cosmological probe. However, due to its

spin-2 nature, it is rather difficult to obtain higher-order summary statistics from shear. While the convergence maps in principle contain the same information as the shear maps (Schneider et al. 2002; Shi et al. 2011), the compression of the lensing signal is greater in convergence maps compared to the shear field, resulting in easier extraction and reduced computational costs, with the caveat that the reconstruction of the convergence maps is not perfectly solved and is a very complex ill-defined inverse problem. Convergence maps emerge as a novel tool, potentially offering additional constraints that complement those derived from the shear field. However, accessing this information is not straightforward and implies the use of a reconstruction method (or mass inversion). In particular, let us note that due to the non-Gaussian nature of the weak-lensing signal at small scales, employing mass-inversion methods with smoothing or de-noising for regularization may not be optimal (Starck et al. 2021; Jeffrey et al. 2020).

The objective of this paper is to present, for the first time, the prediction of the wavelet ℓ_1 -norm derived from theoretical predictions of the PDF of convergence maps. The paper is organized as follows: In Sect. 2.1, we begin by revisiting weak lensing convergence, followed by an introduction to the wavelets and wavelet ℓ_1 -norm in Sect. 2. This is followed by the introduction of the LDT formalism for the κ -PDF and extending this to the wavelet coefficients, in Sect. 3. Section 3.3 delves into the derivation of this wavelet ℓ_1 -norm for the wavelet coefficients from theory. Subsequently, we present and discuss the results in Sect. 4, concluding with the summarizing of our findings in Sect. 5.

2. Wavelet ℓ_1 -norm: definition and measurements

We introduce in this section first the expression for the convergence maps and move to a more general definition of the wavelets and the wavelet ℓ_1 -norm and see how it is related to the PDF.

2.1. Convergence maps

Let us start with the expression for convergence, which is given by a projection of density along the comoving coordinates, weighted by a lensing kernel involving the comoving distances. It is given by (Mellier 1999)

$$\kappa(\boldsymbol{\theta}) = \int_0^{\chi_s} d\chi \omega(\chi, \chi_s) \delta(\chi, \mathcal{D}\boldsymbol{\theta}), \quad (1)$$

where χ is the comoving radial distance – χ_s the radial distance of the source – that depends on the cosmological model, and \mathcal{D} is the comoving angular distance given by

$$\mathcal{D}(\chi) \equiv \begin{cases} \frac{\sin(\sqrt{K}\chi)}{\sqrt{K}} & \text{for } K > 0 \\ \chi & \text{for } K = 0, \\ \frac{\sinh(\sqrt{-K}\chi)}{\sqrt{-K}} & \text{for } K < 0 \end{cases}, \quad (2)$$

with K the constant space curvature. The lensing kernel ω is defined as

$$\omega(\chi, \chi_s) = \frac{3\Omega_m H_0^2}{2c^2} \frac{\mathcal{D}(\chi) \mathcal{D}(\chi_s - \chi)}{\mathcal{D}(\chi_s)} (1 + z(\chi)), \quad (3)$$

where, c is the speed of light, Ω_m the matter density parameter and H_0 is the values of bubble constant at redshift $z = 0$. The shear field $\gamma(\theta)$ which is interpretable directly from the observation is related to the weak lensing convergence κ through mass inversion (Starck et al. 2006; Martinet et al. 2015). The convergence mass maps are in principle constructed only up to a mass sheet degeneracy. However, constructing a mass map by convolving the κ map with a radically symmetrical compensated filter, makes the statistics insensitive to mass sheet degeneracy.

2.2. Wavelets

A wavelet transform enables us to decompose an image κ into different maps called wavelet coefficients w_{θ_j} , i.e. $\mathcal{W}_\kappa = \{w_{\theta_1}, \dots, w_{\theta_j}, \dots, w_{\theta_J}\}$ where θ_j is the angular scale, and θ_J is the largest scale used in the analysis. The wavelet coefficients are the values of the wavelet scales at the pixel coordinates (x, y) . Considering a wavelet function Υ , and noting $\Upsilon_{\theta_j, x, y}(m, n) = \Upsilon\left(\frac{m-x}{\theta_j}, \frac{n-y}{\theta_j}\right)$ the dilated wavelet function at scale θ_j and at spatial location (x, y) , the wavelet coefficients w_{θ_j} are computed as the inner products

$$\begin{aligned} w_{\theta_j}(x, y) &= \langle \kappa, \Upsilon_{\theta_j, x, y} \rangle \\ &= \sum_m \sum_n \kappa(m, n) \Upsilon\left(\frac{m-x}{\theta_j}, \frac{n-y}{\theta_j}\right), \end{aligned} \quad (4)$$

The wavelet function Υ is often chosen to be derived from the difference of two resolutions, for example as $\Upsilon(x, y) = 4\xi(2x, 2y) - \xi(x, y)$ as utilized in the starlet wavelet transform (Starck et al. 2015), where the function ξ is called the scaling function, typically a low-pass filter. In our case, we write the wavelet coefficients as

$$w_{\theta_j}(x, y) = \langle \kappa, \xi_{\theta_{j+1}, x, y} \rangle - \langle \kappa, \xi_{\theta_j, x, y} \rangle, \quad (5)$$

with $\xi_{\theta_j, x, y}(m, n) = \xi\left(\frac{m-x}{\theta_j}, \frac{n-y}{\theta_j}\right)$. Employing dyadic scales, i.e. $\theta_j = 2^{j-1}\theta_1$, enables us to have very fast algorithms through the use of a filter bank. See Starck et al. (2015) for more details.

A wavelet acts as a mathematical function localized in both the spatial and the Fourier domains, thus suitable for analysing the lensing signal's structures at various scales. An important advantage of wavelet analysis, compared to a standard multi-resolution analysis through the use of a set of Gaussian functions of different sizes, is that it decorrelates the information. As an example, Ajani et al. (2023) have shown that the covariance matrix derived from a wavelet peak count analysis was almost diagonal, and neglecting the off-diagonal terms has little impact on the cosmological parameters estimation. This would not be the case with a multi-scale Gaussian analysis. Other advantages are that very fast algorithms exist allowing us to compute all scales with a low complexity, and also that wavelet functions are exactly equivalent to traditional weak-lensing aperture mass functions which have been used for decades (Leonard et al. 2012) (aperture mass is just the convergence/shear within a compensated filters, which is one property of wavelets). Several statistics have been derived from wavelet coefficients in the past, such as cumulants (up to order 6) (Fageot et al. 2014) or peak counts (Ajani et al. 2020). It has recently been shown (Ajani et al. 2021) that the ℓ_1 -norm of the wavelet scales is very efficient in constraining cosmological parameters. In Ajani et al. (2023), a toy model was utilized, incorporating a mock source catalogue for weak lensing and a mock lens catalogue for galaxy clustering sourced from

the cosmo-SLICS ((Harnois-Déraps et al. 2019)) simulations to mimic the KiDS-1000 data survey properties described in Giblin et al. (2018) and Hildebrandt et al. (2021). The study examined forecasts concerning the matter density parameter Ω_m , the matter fluctuation amplitude σ_8 , the dark energy equation of state w_0 , and the reduced Hubble constant h . It was observed that the wavelet ℓ_1 -norm demonstrated superior performance compared to peaks, multi-scale peaks, or a combination thereof (Ajani et al. 2023). Therefore, we propose to build the theory for wavelet ℓ_1 -norm, which could be used for constraining the cosmological parameters with upcoming surveys.

2.3. Wavelet ℓ_1 -norm

To measure the wavelet ℓ_1 -norm from a κ map, we first obtain the wavelet scale by convolving the map with the wavelet function, as given in Eq. 5.

We then compute a histogram of the values of the wavelet scale at each pixel coordinate, $w_{\theta_j}(x, y)$, using a specific binning with bin edges denoted $\{B_i\}_{1 \leq i \leq N}$.

One can then obtain the *normalised*¹ wavelet ℓ_1 -norm by extracting the ℓ_1 -norm of the histogram such that,

$$\ell_1^{\theta_j, i} = \sum_{k=1}^{\#coef(S_{\theta_j, i})} |S_{\theta_j, i}[k]| / N / \Delta B, \quad (6)$$

where the set of coefficients at scale θ_j and amplitude bin i , $S_{\theta_j, i} = \{w_{\theta_j} / w_{\theta_j}(x, y) \in [B_i, B_{i+1}]\}$, depicts the wavelet coefficients w_{θ_j} having an amplitude within the bin $[B_i, B_{i+1}]$, and the pixel indices are given by (x, y) and N is the total number of pixels and ΔB is the uniform bin width. In other words, for each bin, the number of pixels k , that fall in the bin is collected and the absolute values of these pixels are summed to obtain the ℓ_1 -norm at this bin i .

As we already highlighted before, this definition enables us to gather the data represented by the absolute values of every pixel of the map, rather than solely describing it through the identification of local minima or maxima. It has the advantage of being a multiscale approach. In addition, the robustness of ℓ_1 -norm statistics is also well established for decades in the statistical literature (Huber 1987; Giné et al. 2003).

It turns out that the ℓ_1 -norm of the wavelet coefficients can be related directly to the PDF of the wavelet coefficients via the following relation

$$\ell_1^{\theta_j, i} = P(w_j)^i \times |B^i|, \quad (7)$$

which states that the ℓ_1 -norm for a given scale j and at a given bin i (B_i) can be related to its PDF by multiplying the PDF value of the bin i by the absolute value of the bin i .

2.4. Gaussian ℓ_1 -norm

Let us now look at the anticipated wavelet ℓ_1 -norm expected from a Gaussian distribution. The generic shape of a wavelet ℓ_1 -norm obtained from a Gaussian PDF

$$P(x) = \frac{1}{\sigma \sqrt{2\pi}} \exp\left(-\frac{1}{2} \left(\frac{x-\mu}{\sigma}\right)^2\right) \quad (8)$$

¹ In the literature, the common practice has been to use an unnormalised version of the ℓ_1 -norm, but for an easier comparison with prediction and simulation we choose here to normalize this quantity. For the sake of simplicity, we will call it ℓ_1 -norm in this paper.

with mean $\mu = 0$ and $\sigma = 0.1$ using the relation shown in Eq. (7) is demonstrated in Fig. 1.

Here, we see that the height of the two peaks obtained for the wavelet ℓ_1 -norm for the Gaussian (blue solid line) distribution are equal as expected. But, as the Universe evolves, non-linearities develop, which means that the convergence field κ that we are interested in can no longer be modelled using a Gaussian model. These non-linearities would lead to asymmetry which would also be evident from the peaks of the wavelet ℓ_1 -norm, which will no longer be corresponding. This is demonstrated in Fig. 1 for a test case scenario, where we have applied a non-linear exponential transformation, to the Gaussian field to obtain a non-Gaussian field (orange solid line) and obtained the PDF and the ℓ_1 -norm. Here we would like to emphasize that the usual way to extract this non-linear information is either by relying on heavy \mathcal{N} -body simulations or by using an approximation, as is done in (Tessore et al. 2023). But, thanks to LDT, we now have a theoretically motivated way to obtain the PDF in the mildly non-linear regime, using which we will show in this paper that we can also obtain the wavelet ℓ_1 -norm in the mildly non-linear regime.

3. Large Deviation Theory formalism

Let us now, look at the application of the LDT to the convergence field. LDT, as explored in earlier works (Varadhan 1984), examines the rate at which the probabilities of specific events exponentially decrease as a key parameter of the problem undergoes variation. To see how to derive the wavelet ℓ_1 -norm based on the LDT formalism, we first need to recap how to obtain the PDF from the LDT formalism.

3.1. LDT for the matter field

The application of LDT to the field of Large Scale Structure cosmology has been systematically developed in recent years and will be applied in the specific context of cosmic shear observations in this work. (Bernardeau & Reimberg 2016) clarified the application of the theory to the cosmological density field, establishing its link to earlier studies focused on cumulant calculations and modelling the matter PDF through perturbation theory and spherical collapse dynamics (Valageas 2002; Bernardeau et al. 2014). Barthelemy et al. (2020) then provided an LDT-based prediction for the top-hat-filtered weak-lensing convergence PDF on mildly nonlinear scales, building upon earlier work by (Bernardeau & Valageas 2000).

A more detailed derivation of the specific equations used is presented in the Appendix A for the interested readers. In this section, we simply recall the main equation that will then be needed for us to derive the wavelet ℓ_1 -norm prediction.

Within the context of the application of LDT in Cosmology, there are three main steps involved. The first is the derivation of the rate function, which is obtained directly from the first principles of Cosmology. Using the contraction principle in the LDT formalism, we can connect the statistics of the late-time non-linear densities to the earlier time density field as soon as the most likely mapping between the two is known. Previous works have shown that assuming spherical collapse for this mapping provides us with a very accurate prediction for cosmic field PDF (density, velocity, convergence, ...).

In particular, the result for convergence reads

$$P(\kappa) = \int_{-i\infty}^{+i\infty} \frac{d\lambda}{2\pi i} \exp(-\lambda\kappa + \phi_{\kappa,\theta}(\lambda)) \quad (9)$$

where, $P(\kappa)$ is the PDF of the convergence field κ , and $\phi_{\kappa,\theta}$ is the cumulant generating function (CGF) of the field κ at angular scale θ . The derivation of the CGF in the above equation and PDF from there is explained in more detail in Appendix A.

3.2. Extending to wavelet coefficients

From the PDF, we can now compute the ℓ_1 -norm. As was given in the Sect. 2, a wavelet can be written as a function of scaling functions. Though various wavelet filters exists in literature, in this study, we employ a function of concentric disks to construct the wavelet filter Υ_{θ_1} .

The scaling function ξ is then given by a spherical top hat filter and is given by

$$\hat{\xi}_{\theta_1} = 2J_1(\theta_1 l) / (\theta_1 l) \quad (10)$$

where J_1 is the first Bessel function of the first kind. This is applied, as shown in Eq. (5), to obtain our compensated filter. In Fig. 2, we show the compensated filter (black solid line) that is used in this work, which is given as a function of two scaling functions (orange and blue solid lines) at different scales.

We now apply the LDT formalism described previously to the wavelet coefficients described in Eq. (5) and obtain the PDF of the wavelet coefficients (w_{θ_1}) by using the scales $\theta_1, \theta_2 = 2\theta_1$ as

$$P(w_{\theta_1}) = \int_{-i\infty}^{+i\infty} \frac{d\lambda}{2\pi i} \exp(-\lambda w_{\theta_1} + \phi_{w_{\theta_1}}(\lambda)). \quad (11)$$

We refer the readers to Appendix A, for more details on the derivation of the CGF in the above equation and the resulting PDF. We emphasize that w_{θ_1} is essentially the standard aperture mass aperture mass defined on the convergence field using a difference of two top-hat filters, as was discussed previously.

3.3. Wavelet ℓ_1 -norm predicted via Large Deviation Theory

In the previous sections, we saw how the LDT formalism can be applied to derive the PDF of the wavelet coefficients. We will now see how to derive the wavelet ℓ_1 -norm from the PDF of the wavelet coefficients $P(w_{\theta_1})$. This wavelet ℓ_1 -norm given in Eq. (6), which is the sum of the absolute values of the pixels in each bin, is equivalent to multiplying the counts/PDF value by the absolute value of the bin it corresponds to, as is given in Equation (7). Extending this to the PDF of the wavelet coefficients from the LDT formalism, we get the final equation for bin i

$$\ell_1^i = P^i(w_{\theta_1}) \times |w_{\theta_1}^i|. \quad (12)$$

As a first approximation, one can assume that the PDF is Gaussian, which is the case when we consider large scale or early time in the standard model of Cosmology. In the subsequent section, we look at obtaining the ℓ_1 -norm for a Gaussian case first and then highlight the motivation to go beyond Gaussian models.

4. Confronting ℓ_1 -norm prediction to simulations

4.1. Measurements from simulation

To demonstrate the accuracy of the theory for realistic surveys, we compare our prediction results with full-sky simulations of Takahashi et al. (2017) to avoid additional errors from small-scale patch sizes. The simulations of Takahashi et al. (2017) provides full sky lensing maps at a fixed cosmology ² each for two

² http://cosmo.phys.hirosaki-u.ac.jp/takahasi/allsky_raytracing/

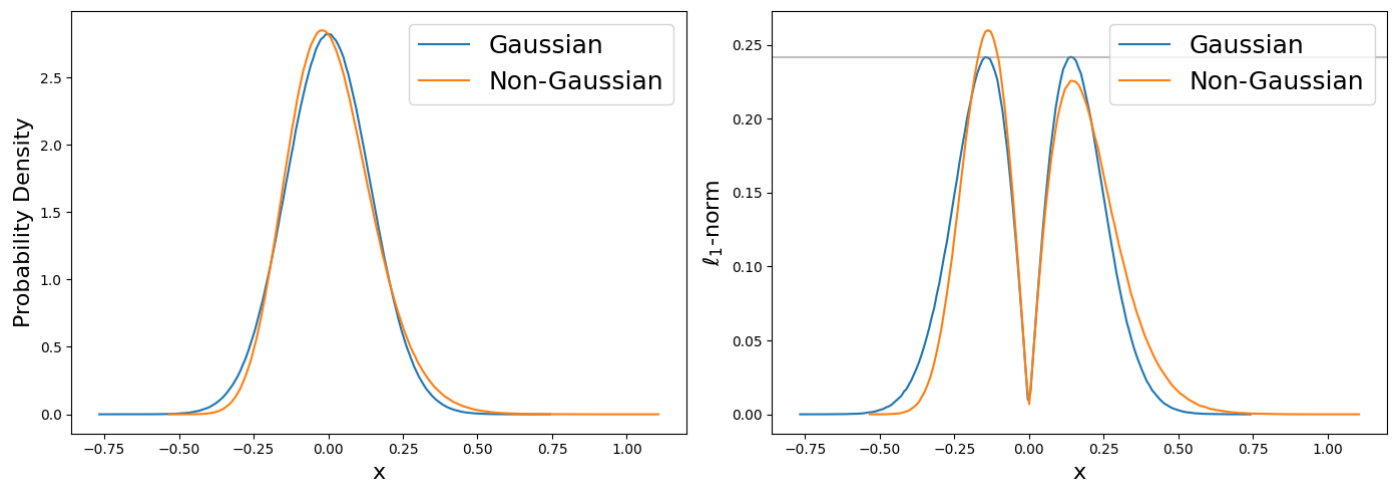


Fig. 1. This figure illustrates the PDF and the ℓ_1 -norm for a Gaussian distribution in blue and the non-Gaussian distribution in orange. On the left, we present the Probability Distribution Function (PDF) for the two distributions, and on the right, we display the derived ℓ_1 -norm of these PDFs. Let us note that the heights of the peaks are the same for a Gaussian distribution but this does not hold for a non-Gaussian PDF.

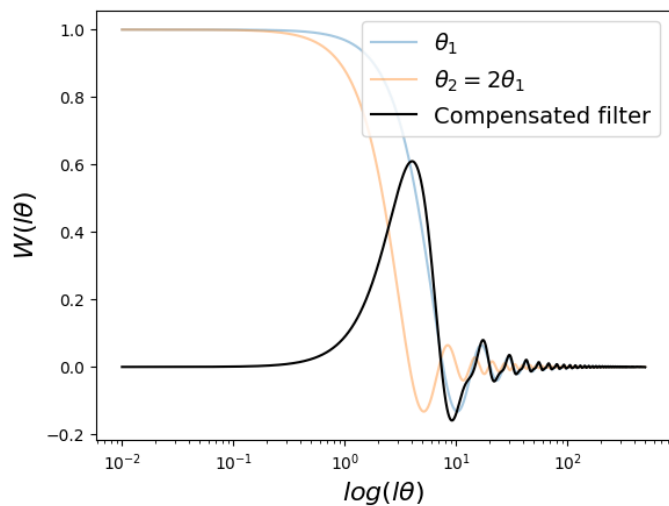


Fig. 2. The compensated filter (depicted by the black solid line) is derived through a difference of two top-hat filters at different scales, as described in Eq. (5) and Eq. (10). The blue and orange solid lines represent the individual spherical filters obtained at radii θ_1 and $\theta_2 = 2\theta_1$, respectively. For visualization purposes, the compensated filter is multiplied by -1 .

grid resolutions: 4096^2 and 8192^2 . The data sets include the full sky maps at intervals of $150h^{-1}$ comoving radial distance from redshifts $z = 0.05$ to 5.3 . We use the simulated convergence maps that are directly provided as products of these simulations. The smoothing of the convergence maps is implemented as a direct convolution of the convergence map with the wavelet filter at a given angular scale. Once the filtered field is obtained, we measure the sum of the absolute values of the pixels of the smoothed κ mass map in linearly spaced bins of the range of κ to obtain the wavelet ℓ_1 -norm.

4.2. Obtaining the prediction

To obtain the prediction of the wavelet ℓ_1 -norm for each of the cosmologies used here, we first use CAMB (Lewis & Challinor 2011) to get the linear and non-linear (Halofit takahashi (Taka-

hashi et al. 2012)) matter power spectra. We also use CAMB to obtain the comoving radial distances $\chi(z)$. The density CGF (Eq. (A.9)) is calculated for redshift slices between $z = 0$ and the source redshift z_s using the full Halofit power spectrum as input. These projected CGFs are then rescaled by the measured variance $\sigma_{M_{ap, sim}}^2$ (see Appendix A for more details), before going through an inverse Laplace transform to get the final PDF. This predicted PDF is used to derive the predicted wavelet ℓ_1 -norm as given in Eq. (12).

4.3. Validating the prediction with simulation

In Figures 3 and 4, we show the predicted wavelet ℓ_1 -norm and the one measured from the simulated convergence map for different source redshifts $z_s \approx 1.2, 1.4, 2.0$ at $\theta = 20'$ and for different scales $\theta = 15', 18', 20'$ at source redshift $z_s = 1.423$ respectively. On the bottom panels, we show the residuals. For comparison, we display the PDF and the residuals of a Gaussian distribution (dash-dot line) with the same mean and variance as the simulation. The Gaussian PDF is obtained using Eq. (8), and the ℓ_1 -norm is derived as explained previously in Eq. (12). In both plots, the x -axis for the residuals is scaled by the standard deviation. The shaded regions in the colors correspond to the 3σ region obtained from the error bars.

The error bars are obtained by taking the standard deviation of the values of the wavelet ℓ_1 -norm for 10 different patches of the full sky Takahashi map in each of the bins.

Let us first concentrate on the Gaussian curves. We see a clear mismatch with the Gaussian prediction as expected since the measurements show a clear asymmetry unless the Gaussian model which by definition is symmetric.

Let us now focus on the LDT prediction that goes beyond the Gaussian regime. In this case, we observe a better agreement between the simulation and the predicted wavelet ℓ_1 -norm results to percent levels (which corresponds to the simulation error bars in shaded area) within the $2 - \sigma$ region around zero on the x -axis. This demonstrates the predictive accuracy of the results derived from the LDT formalism. It is important to note that this $2 - \sigma$ specification refers to the range on the x -axis, rather than representing error bars around the mean signal value.

In these plots, we indeed clearly see that LDT is capable of capturing the asymmetry of the two peaks hence valuable infor-

Table 1. The cumulants (standard deviation σ , skewness S_3) obtained from the PDF from the LDT prediction and the values obtained from the Takahashi simulation at source redshift $z_s \approx 2.05$ for scales 15, 18, and 20 arcminutes. The corresponding PDFs are shown in Figure 4

Data	$\sigma^2 \times 10^{-5}$	S_3
Prediction 15'	2.92	-26.3
Simulation 15'	2.92	-42.8
Prediction 18'	2.61	-25.94
Simulation 18'	2.61	-38.2
Prediction 20'	2.44	-25.7
Simulation 20'	2.44	-35.4

mation about the non-gaussianities. To better assess this aspect, we also show, in Table 1, the cumulants obtained for the three scales at source redshift $z_s = 1.423$. The cumulants shown here are the variance (σ^2) and reduced skewness (S_3) which, given that the mean convergence is zero, are obtained as

$$\sigma^2 = E[\kappa^2] \quad (13)$$

$$S_3 = \frac{E[\kappa^3]}{\sigma^3} \quad (14)$$

where,

$$E[\kappa^n] = \int P(\kappa) \kappa^n d\kappa. \quad (15)$$

From Table 1, we see that the variance from the prediction and simulation for different scales match perfectly, which we expect given the re-scaling by the power spectrum that we perform (see appendix A). As expected from the formalism, we see that the reduced skewness (S_3) increases with decreasing smoothing scale. We also notice that the ℓ_1 -norm for the positive bins is not at all equal to the negative bins, suggesting how prominent the non-Gaussian features of the mass map are in this regime. It was shown in Barthelemy et al. (2020), that the theoretical precision achievable is constrained by the mixing of scales when integrating the density field along the line of sight since highly non-linear scales are not precisely captured by the spherical collapse formalism. Consequently, weak lensing statistical measures are often approached through more phenomenological methods, such as halo models. These models are capable of incorporating baryonic physics, which becomes crucial at smaller scales, as highlighted by Mead et al. (2021). That is also evident when we look at Fig. 3 and Fig. 4, where we do see that the level of accuracy increases as we move to higher redshifts and higher smoothing scales. To bypass this issue, a rising approach is to use the so-called Bernardeau-Nishimichi-Taruya (BNT) transform (Bernardeau et al. 2014), which enables more accurate theoretical predictions by narrowing the range of physical scales contributing to the signal.

4.4. Cosmology dependence of PDF and wavelet ℓ_1 -norm

In this section, we explore the cosmological dependence of the predicted pdf of the wavelet coefficients and ℓ_1 -norm. We would like to emphasize that since the wavelet decomposition is analogous to using an aperture mass map filtering, we henceforth can also call the PDF of the wavelet coefficients as the aperture mass PDF. From the equation of the rate function given in Eq. (A.7), the cosmology dependence of the aperture mass PDF

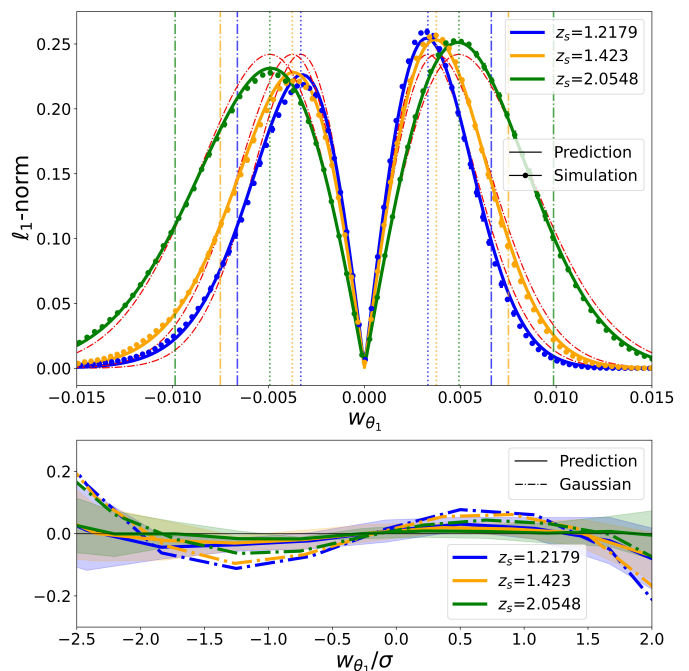


Fig. 3. Top panel: Predicted (solid) ℓ_1 -norm as compared to measurements in simulation (dot markers) for an inner radius $\theta_1 = 20'$ and different source redshifts $z_s = 1.21, 1.43, 2.05$, displayed with blue, orange, and green lines respectively. Red dash-dotted lines show the Gaussian prediction for reference. The vertical dotted and dot-dash lines correspond to the 1σ and 2σ regions around the mean of the w_{θ_1} for each of the case considered. Bottom panel: residual of the prediction relative to the simulation (dotted lines). For reference, the dash-dotted plots illustrate the residual of the ℓ_1 -norm derived from the Gaussian PDF with the same mean and variance as the simulation PDF. The shaded region indicates the 3σ region around the error bars for each redshift. The prediction is in good agreement with the measurements up to approximately 2 sigma and remains within percent levels.

in LDT enters through the scale-dependence of, the non-linear power-spectrum, the dynamics of the spherical collapse and the lensing kernel. Moreover, the presence of massive neutrinos if any also affects the aperture mass as it enters the lensing kernel as given in Eq. (3), by contributing to the total matter density budget. All of this inevitably means that the summary statistics would also be cosmology-dependent. In the context of applying LDT to predict the wavelet ℓ_1 -norm and PDFs, based on the equations introduced above, we could assume that it should be able to efficiently capture the cosmology dependence. Indeed, the cosmology dependence of the one-scale one-point convergence PDF has been studied in detail in Boyle et al. (2021) which showed that LDT captures very accurately the cosmology dependence. In this work, we extend this study for the case of the PDF of the wavelet coefficients and the wavelet ℓ_1 -norm of aperture mass maps. As for the one-scale case, the rate function for the multi-scale also depends on the variance and the dynamics of the spherical collapse, which means that the PDF of the wavelet coefficients would also be expected to depend (similarly) on the cosmology. Additionally, since the wavelet ℓ_1 -norm is directly dependent on the PDF, we could naively expect it to depend on the cosmology too, and encapsulate the dependence.

Since we are interested in obtaining the derivatives with respect to cosmological parameters, we need a simulation suite that is available for different cosmologies. For this, we use the Cosmological Massive Neutrino simulations (MassiveNus) (Liu

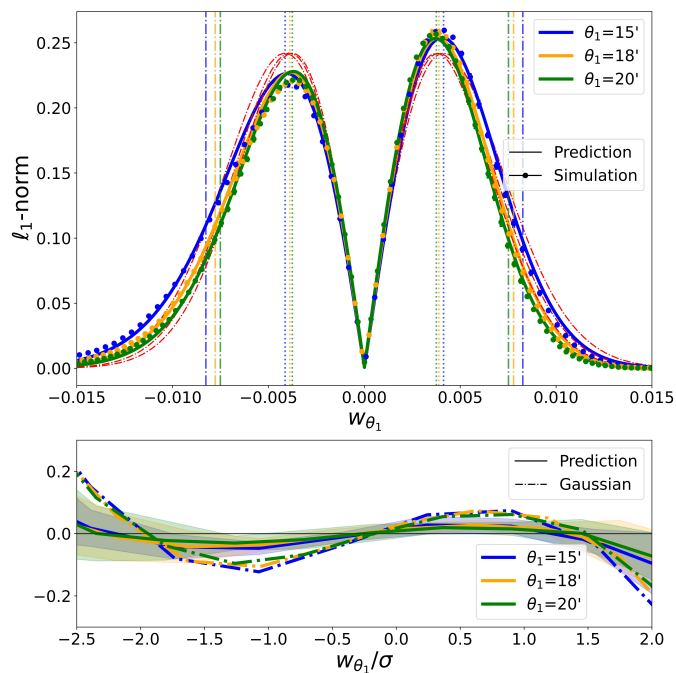


Fig. 4. Top panel: Predicted (solid) ℓ_1 -norm as compared to measurements in simulation (dot markers) for different inner radii $\theta_1 = 15', 18', 20'$ and single source redshift $z_s = 1.43$, displayed with blue, orange, and green lines respectively. Red dash-dotted lines show the Gaussian prediction for reference. The vertical dotted and dot-dash lines correspond to the 1σ and 2σ regions around the mean of the w_{θ_1} for each of the case considered. Bottom panel: residual of the prediction relative to the simulation (dotted lines). For reference, the dash-dotted plots illustrate the residual of the ℓ_1 -norm derived from the Gaussian PDF with the same mean and variance as the simulation PDF. The shaded region indicates the 3σ region around the error bars for each inner radius. The prediction is in good agreement with the measurements up to approximately 2 sigma and remains within percent levels.

et al. 2018) suite to see how well the theory can capture the dependence on cosmology. These simulations are released by the Columbia Lensing Group³. The MassiveNuS simulations encompass 101 different cosmological models at source redshifts $z_s = 0.5, 1.0, 1.5, 2.0, 2.5$, by varying three parameters: the neutrino mass sum M_ν , the total matter density Ω_m , and the primordial power spectrum amplitude A_s . For each redshift, there are 10,000 distinct map realizations generated through random rotation and translation of the initial n-body box then stitched together to reconstruct pseudo-independent light cones that are unlikely to cross the same structures. Each κ map contains 512^2 pixels, covering a total angular area of 12.25 square degrees, spanning a range of $\ell \in [100, 37,000]$ with a pixel resolution of 0.4 arcminutes. The measurement of the wavelet ℓ_1 -norm is obtained using the same process as was described previously in Sec. 4.1. Additionally, the measurement of the PDF is derived from the histogram of the binned and smoothed map. To obtain the derivatives, we use the model with parameters $\Omega_m = 0.30$, $A_s = 2.1 \times 10^{-9}$, and $M_\nu = 0.0$ eV as the fiducial model (model 1b in Liu et al. (2018)) and obtain the derivatives of the PDF for each of the parameters. The different parameters are shown in Table 2. The outcomes are illustrated in Figures 5 to 6. For the derivative with respect to M_ν , we employ a model with the same Ω_m and A_s values but with $M_\nu = 0.0$, eV and then compute the derivative. However, it is important to note that due to resolution

³ <http://columbialensing.org/>

Table 2. The cosmological parameters used to obtain the derivatives of the PDF.

Parameters	lower bound	fiducial	upper bound
Ω_m	0.28	0.3	0.31
$A_s \times 10^{-9}$	2.0	2.1	2.17
M_ν	0.09	0.0	0.11

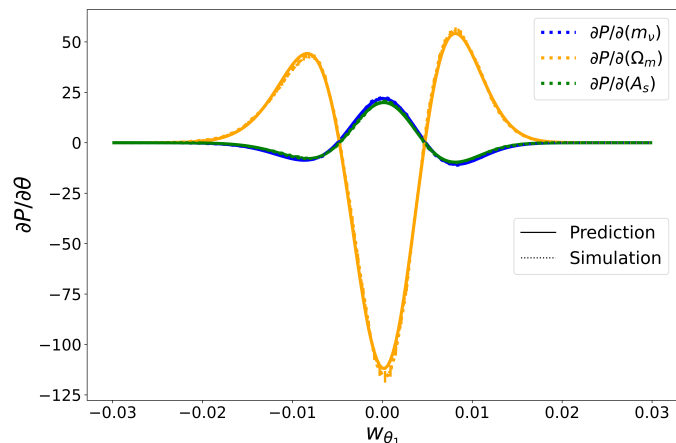


Fig. 5. Derivative of the PDF with respect to M_ν (blue), Ω_m (orange) and A_s (green). The solid lines show the derivatives obtained from prediction and the dotted lines show the derivatives from simulation. It is obtained at source redshift $z_s = 2$ and inner radius $\theta_1 = 22.5'$. The results for simulation are obtained from the MassiveNuS simulation suite, by averaging the results over 10,000 simulations.

and finite volume effects, the simulation power spectrum of the convergence maps exhibits a deficit in power at high ℓ , which does influence us much because of the scales we are looking at, and at low ℓ which invites caution when choosing our largest scales. We typically try to maintain a factor of 20 between the physical scale of the box and the largest physical scale probed by our filters.

It is evident from Figures 5 and 6, that the prediction effectively captures the changes in cosmology, demonstrating good agreement with the results. The errorbars are obtained by taking the error of mean of 3000 simulations, which are also used to obtain the mean of the measurements.

As demonstrated in Boyle et al. (2021) for the case of a 1-cell PDF, our results here demonstrate that the theory captures well the effects of adding massive neutrinos to cosmology, extending the results also for the PDF of the wavelet coefficients.

4.5. Reproducible research

In the spirit of open research, the code related to reproducing the plots in this paper is available at [github](https://github.com). A part of this Python code that computes the aperture mass/wavelet coefficient PDF was inspired by the public Mathematica code L2DT used in Barthelemy et al. (2021).

5. Discussion and Conclusions

In this work, we have used the LDT to build upon the previous work by Barthelemy et al. (2021) and introduced a formalism to predict the ℓ_1 -norm of the wavelet coefficients of the lensing field

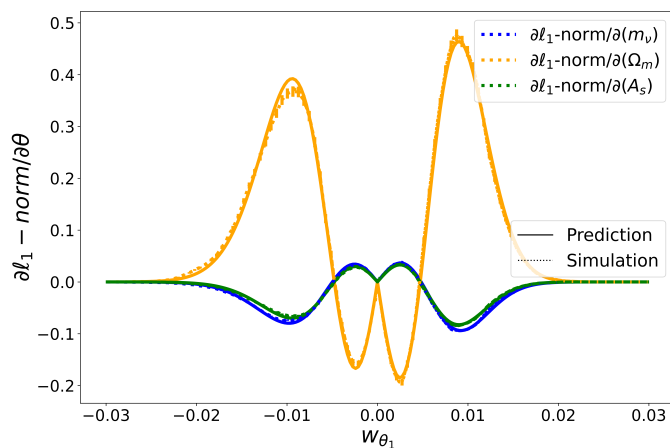


Fig. 6. Derivative of the wavelet ℓ_1 -norm with respect to M_v (blue), Ω_m (orange) and A_s (green). The solid lines show the derivatives obtained from prediction, and the dotted lines show the derivatives from simulation. The predicted wavelet ℓ_1 -norm is derived from the predicted PDF as was explained in previous sections. It is obtained at source redshift $z_s = 2$ and inner radius $\theta_1 = 22.5'$. The results for simulation are obtained from the MassiveNus simulation suite, by averaging the results over 10,000 simulations.

and their cosmological dependence for any given redshift and scales as long as they are in the mildly non-linear regime. The approach of Barthelemy et al. (2021) incorporates the geometric and time-evolution aspects within the light cone by considering that the correlations of the underlying matter density field along the line of sight are negligible compared to transverse directions. This Limber approximation enables us to treat redshift slices as statistically independent. It was found that the most likely non-linear dynamics of the matter density field filtered in concentric disks can be well approximated for small variances by the cylindrical collapse model, thus allowing for LDT to be applied in this context. From there, because the wavelet ℓ_1 -norm can be directly related to the multi-scale one-point statistics of the convergence, we have shown in this paper that a theory-based prediction for the wavelet ℓ_1 -norm is tractable.

The robust validation of our predictions against the simulations, in Figs. 4 and 3, highlighted the reliability and applicability of our theoretical framework. Specifically, our theory aligns with the simulations within percent level accuracy across the examined range of source redshifts $z_s \approx 1 - 2$ and angular scales $\theta_1 \approx 15 - 20$. This quantitative assessment affirms the predictive precision of our model. Obviously going towards smaller scales or lower redshifts would lead to a larger departure between simulations and theory.

Figure 6, further emphasizes the cosmological dependencies and the very good performance of the theoretical prediction, when compared with that of the simulation. Since the simulations have validated the theoretical predictions, it suggests that our model could be applied to investigate a broad range of cosmological parameters, while bypassing the need for high computing resources and providing a theoretical tool for cosmology inference that is robust and fast, without the loss of quality. This paves the way for a more comprehensive and faster forecast analysis based on theory without having to rely on expensive numerical simulations. In addition, we noted in Figures 5 and 6 that there is numerical noise in the simulation results (fitted lines). This can lead to biases in parameter estimations when using the simulation data. The use of a theory-based approach has

the added benefit of reducing the artificial biases in parameter inference, which was also noted in Boyle et al. (2021).

Another point to be noted is, that although lower source redshifts are expected to generate more non-Gaussian information, this also pushes the model deeper into the nonlinear regime. This effect can be mitigated by adjusting the smoothing scale accordingly. We would also like to emphasize the usefulness of the wavelet coefficients of the convergence maps, instead of the convergence maps or the shear maps directly. Convergence maps already reduce computation expense, because of the presence of a more compressed lensing signal when compared to the shear map. However, the use of the wavelet scales and/or coefficients provides us with a multi-scale analysis method, which is well suited to constrain the cosmology.

Moreover, wavelet coefficients are invariant under the mass sheet degeneracy, which renders the link to the measured shear data more straightforward.

More generally, one of the issues with the theoretical modelling of weak lensing we currently face is the mixing of (non-linear) scales that is inherent to such quantities projected along the past light cone and makes standard perturbative approaches inaccurate even on relatively large angular scales. (Bernardeau et al. 2014) To overcome this issue, an emerging method is to utilize the BNT transform which allows for more precise theoretical predictions by reducing the range of physical scales that contribute to the signal. This could be applied in our context and enables even more accurate predictions for analysing tomographic surveys. Investigating the performance of this approach is left for future works, together with the impact of systematics that would require to devise specific simulated data, as well as additional theoretical development.

We conclude that the novel approach for obtaining the theoretical prediction of the wavelet ℓ_1 -norm summary statistic proposed here presents several advantages in the realm of cosmological parameter inference: i) it provides a fast (~ 1 minute) calculation; ii) it does not rely on a heavy numerical simulation; iii) it captures well the cosmology dependence; and iv) wavelet ℓ_1 -norm could lead to competitive or even tighter constraints as demonstrated by previous works. We hence have at hand a promising method that could enable a comprehensive multi-scale analysis of cosmic shear datasets in the mildly non-linear regime.

Acknowledgements. This work was funded by the TITAN ERA Chair project (contract no. 101086741) within the Horizon Europe Framework Program of the European Commission, and the Agence Nationale de la Recherche (ANR-22-CE31-0014-01 TOSCA and ANR-18-CE31-0009 SPHERES). AB's work is supported by the ORIGINS excellence cluster. We thank Jia Liu and the Columbia Lensing group (<http://columbialensing.org>) for making the MassiveNus (Liu et al. 2018) simulations available. The creation of these simulations is supported through grants NSF AST-1210877, NSF AST-140041, and NASA ATP-80NSSC18K1093. We thank New Mexico State University (USA) and Instituto de Astrofísica de Andalucía CSIC (Spain) for hosting the Skies & Universes site for cosmological simulation products. We also thank C. Uhlemann, O. Friedrich, Lina Castiblanco, and Martin Kilbinger for insightful discussions.

References

- Ajani, V., Harnois-Déraps, J., Pettorino, V., & Starck, J.-L. 2023, A&A, 672, L10
- Ajani, V., Peel, A., Pettorino, V., et al. 2020, Phys. Rev. D, 102, 103531
- Ajani, V., Starck, J.-L., & Pettorino, V. 2021, A&A, 645, L11
- Bacon, D. J., Refregier, A. R., & Ellis, R. S. 2000, MNRAS, 318, 625
- Bartelmann, M. & Maturi, M. 2017, Scholarpedia, 12, 32440
- Barthelemy, A., Codis, S., & Bernardeau, F. 2021, MNRAS, 503, 5204
- Barthelemy, A., Codis, S., Uhlemann, C., Bernardeau, F., & Gavazzi, R. 2020, MNRAS, 492, 3420
- Bernardeau, F., Colombi, S., Gaztañaga, E., & Scoccimarro, R. 2002, Physics Reports, 367, 1–248

- Bernardeau, F., Nishimichi, T., & Taruya, A. 2014, *MNRAS*, 445, 1526
- Bernardeau, F., Pichon, C., & Codis, S. 2014, *Phys. Rev. D*, 90, 103519
- Bernardeau, F. & Reimberg, P. 2016, *Phys. Rev. D*, 94, 063520
- Bernardeau, F. & Valageas, P. 2000, *A&A*, 364, 1
- Bernardeau, F. & Valageas, P. 2001, Construction of the one-point PDF of the local aperture mass in weak lensing maps
- Boyle, A., Uhlemann, C., Friedrich, O., et al. 2021, *MNRAS*, 505, 2886
- Cheng, S. & Ménard, B. 2021, *MNRAS*, 507, 1012
- Euclid Collaboration, Deshpande, A. C., Kitching, T., et al. 2024, *A&A*, 684, A138
- Fageot, J., Bostan, E., & Unser, M. 2014, in 2014 IEEE International Conference on Image Processing (ICIP), 6096–6100
- Gatti, M., Chang, C., Friedrich, O., et al. 2020, *MNRAS*, 498, 4060
- Giblin, B., Heymans, C., Harnois-Déraps, J., et al. 2018, *MNRAS*, 480, 5529
- Giné, E., Mason, D. M., & Zaitsev, A. Y. 2003, *The Annals of Probability*, 31, 719
- Harnois-Déraps, J., Giblin, B., & Joachimi, B. 2019, *A&A*, 631, A160
- Heymans, C., Van Waerbeke, L., Miller, L., et al. 2012, *MNRAS*, 427, 146
- Hildebrandt, H., van den Busch, J. L., Wright, A. H., et al. 2021, *A&A*, 647, A124
- Hildebrandt, H., Viola, M., Heymans, C., et al. 2017, *MNRAS*, 465, 1454
- Huber, P. J. 1987, *Computational statistics & data Analysis*, 5, 255
- Huterer, D. 2010, *General Relativity and Gravitation*, 42, 2177–2195
- Ingoglia, L., Covone, G., Sereno, M., et al. 2022, *MNRAS*, 511, 1484
- Ivezić, Ž., Kahn, S. M., Tyson, J. A., et al. 2019, *ApJ*, 873, 111
- Jeffrey, N., Lanusse, F., Lahav, O., & Starck, J.-L. 2020, *MNRAS*, 492, 5023
- Kaiser, N., Wilson, G., & Luppino, G. A. 2000, Large-Scale Cosmic Shear Measurements
- Kilbinger, M. 2015, *Reports on Progress in Physics*, 78, 086901
- Kilbinger, M. 2018, Cosmological parameters from weak cosmological lensing
- Kratochvil, J. M., Lim, E. A., Wang, S., et al. 2012, *Phys. Rev. D*, 85, 103513
- Kruse, G. & Schneider, P. 1999, *MNRAS*, 302, 821
- Laureijs, R., Amiaux, J., Arduini, S., et al. 2011, Euclid Definition Study Report
- Leonard, A., Pires, S., & Starck, J.-L. 2012, *MNRAS*, 423, 3405–3412
- Lesgourgues, J. & Pastor, S. 2012, *Advances in High Energy Physics*, 2012, 1–34
- Lewis, A. & Challinor, A. 2011, *CAMB: Code for Anisotropies in the Microwave Background*, Astrophysics Source Code Library, record ascl:1102.026
- Li, Z., Liu, J., Zorrilla Matilla, J. M., & Coulton, W. R. 2019, *Phys. Rev. D*, 99, 063527
- Lin, C.-A. & Kilbinger, M. 2015, *A&A*, 583, A70
- Liu, J., Bird, S., Matilla, J. M. Z., et al. 2018, *Journal of Cosmology and Astroparticle Physics*, 2018, 049
- Liu, J. & Madhavacheril, M. S. 2019, *Phys. Rev. D*, 99, 083508
- Liu, J., Petri, A., Haiman, Z., et al. 2015a, *Phys. Rev. D*, 91, 063507
- Liu, X., Pan, C., Li, R., et al. 2015b, *MNRAS*, 450, 2888
- Loureiro, A., Whiteaway, L., Sellentin, E., et al. 2023, *The Open Journal of Astrophysics*, 6
- Mandelbaum, R. 2018, *Annual Review of Astronomy and Astrophysics*, 56, 393–433
- Mandelbaum, R. & Collaboration, H. S.-C. H. 2017, in *American Astronomical Society Meeting Abstracts# 229*, Vol. 229, 226–02
- Martinet, N., Bartlett, J. G., Kiessling, A., & Sartoris, B. 2015, *A&A*, 581, A101
- Mead, A. J., Brieden, S., Tröster, T., & Heymans, C. 2021, *MNRAS*, 502, 1401
- Mellier, Y. 1999, *ARA&A*, 37, 127
- Mukhanov, V. 2005, *Physical Foundations of Cosmology* (Cambridge: Cambridge Univ. Press)
- Munshi, D., Valageas, P., van Waerbeke, L., & Heavens, A. 2008, *Phys. Rep.*, 462, 67
- Parroni, C., Cardone, V. F., Maoli, R., & Scaramella, R. 2020, *A&A*, 633, A71
- Peebles, P. J. E. 1980, The large-scale structure of the universe
- Peel, A., Lin, C.-A., Lanusse, F., et al. 2017, *A&A*, 599, A79
- Peel, A., Pettorino, V., Giocoli, C., Starck, J.-L., & Baldi, M. 2018, *A&A*, 619, A38
- Petri, A. 2016, *Astronomy and Computing*, 17, 73
- Reimberg, P. & Bernardeau, F. 2018, *Phys. Rev. D*, 97
- Rizzato, M., Benabed, K., Bernardeau, F., & Lacasa, F. 2019, *MNRAS*, 490, 4688
- Schneider, P., van Waerbeke, L., Kilbinger, M., & Mellier, Y. 2002, *A&A*, 396, 1
- Semoloni, E., Schrabback, T., van Waerbeke, L., et al. 2011, *MNRAS*, 410, 143
- Shi, X., Schneider, P., & Joachimi, B. 2011, *A&A*, 533, A48
- Starck, J.-L., Murtagh, F., & Fadili, J. 2015, *Sparse image and signal processing: Wavelets and related geometric multiscale analysis*, second edition, 1–423
- Starck, J. L., Pires, S., & Réfrégier, A. 2006, *A&A*, 451, 1139
- Starck, J. L., Themelis, K. E., Jeffrey, N., Peel, A., & Lanusse, F. 2021, *A&A*, 649, A99
- Takada, M. & Jain, B. 2004, *MNRAS*, 348, 897
- Takahashi, R., Hamana, T., Shirasaki, M., et al. 2017, *The Astrophysical Journal*, 850, 24
- Takahashi, R., Sato, M., Nishimichi, T., Taruya, A., & Oguri, M. 2012, *ApJ*, 761, 152
- Takahashi, R., Sato, M., Nishimichi, T., Taruya, A., & Oguri, M. 2012, *The Astrophysical Journal*, 761, 152
- Tessore, N., Loureiro, A., Joachimi, B., von Wietersheim-Kramsta, M., & Jeffrey, N. 2023, *The Open Journal of Astrophysics*, 6
- Touchette, H. 2009, *Physics Reports*, 478, 1
- Troxel, M. & Ishak, M. 2015, *Physics Reports*, 558, 1, the intrinsic alignment of galaxies and its impact on weak gravitational lensing in an era of precision cosmology
- Uhlemann, C., Pichon, C., Codis, S., et al. 2018, *MNRAS*, 477, 2772
- Valageas, P. 2002, *A&A*, 382, 412
- Varadhan, S. R. S. 1984, *Large Deviations and Applications* (Society for Industrial and Applied Mathematics)
- Waerbeke, L. V., Mellier, Y., Erben, T., et al. 2000, Detection of correlated galaxy ellipticities on CFHT data: first evidence for gravitational lensing by large-scale structures
- Weinberg, D. H., Mortonson, M. J., Eisenstein, D. J., et al. 2013, *Physics reports*, 530, 87

Appendix A: Large Deviation Theory

Appendix A.1: LDT for the matter field

The computations detailed in this section draw heavily from the formulations provided in [Boyle et al. \(2021\)](#) and [Barthelemy et al. \(2021\)](#). Here, we will succinctly restate the key equations and direct the reader to the comprehensive treatments in [Boyle et al. \(2021\)](#), [Barthelemy et al. \(2021\)](#), and [Reimberg & Bernardeau \(2018\)](#).

The LDT, as explored in earlier works [Varadhan \(1984\)](#), examines the rate at which the probabilities of specific events diminish as a key parameter of the problem undergoes variation. Widely applied in various mathematical and theoretical physics domains, this theory is particularly prominent in statistical physics, covering both equilibrium and non-equilibrium systems. For a detailed overview, readers are referred to [Touchette \(2009\)](#).

The utilization of the Large Deviation Principle (LDP) in the domain of Large Scale Structure cosmology has been systematically developed in recent years and will be applied in the specific context of cosmic shear observations in this work. [Bernardeau & Reimberg \(2016\)](#) clarified the application of the theory to the cosmological density field, establishing its link to earlier studies focused on cumulant calculations and modelling the matter PDF through perturbation theory and spherical collapse dynamics ([Valageas \(2002\)](#); [Bernardeau et al. \(2014\)](#)). [Barthelemy et al. \(2020\)](#) provided an LDT-based prediction for the top-hat-filtered weak-lensing convergence PDF on mildly nonlinear scales, building upon earlier work by [Bernardeau & Valageas \(2000\)](#).

The LDP applied to the matter density field relies on three key aspects:

- Defining a rate function for variables in the initial field configuration. In this context, we opt for Gaussian initial conditions and establish their covariance matrix.
- Describing the relationship between the initial field configuration (representing the mass profile) and the resulting mass profile, based on 2D cylindrical collapse or a suitable approximation.
- Using these foundations to express observable quantities, like a map created with a specific filter, as functional expressions that depend on both the final and initial mass profile.

A LDP for matter densities at multiple scales (indexed by i) $\{\rho_i^\epsilon\}$, $1 \leq i \leq N$ with joint PDF $\mathcal{P}_\epsilon(\{\rho_i^\epsilon\})$ is satisfied if the following limit exists

$$\psi_{\{\rho_i^\epsilon\}}(\{\rho_i^\epsilon\}) = -\lim_{\epsilon \rightarrow 0} \epsilon \log[\mathcal{P}_\epsilon(\{\rho_i^\epsilon\})]. \quad (\text{A.1})$$

If such limit exists, $\psi_{\{\rho_i^\epsilon\}}$ is called the rate function.

Here, ϵ is a driving parameter, indicating the set of random variables linked to a specific evolutionary process. For the matter density field at a single scale, this parameter reflects its variance, marking time from initial stages to later times. In joint statistics involving concentric disks of matter, the common driving parameter can be selected as the variance at any radius or scale. This consistency arises because all variances behave the same as they approach zero. In this limit, they directly scale with the square of the growth rate of structure in the linear regime.

If LDP holds for the random variable ρ_i , then Varadhan's theorem allows us to connect its Scaled Cumulant Generating Function (SCGF) φ_{ρ_i} to the rate function ψ_{ρ_i} through a Legendre-Fenchel transform

$$\varphi_{\{\rho_i\}}(\{\lambda_i\}) = \sup_{\{\rho_i\}} \left[\sum_i \lambda_i \rho_i - \psi_{\{\rho_i\}}(\{\rho_i\}) \right]. \quad (\text{A.2})$$

This Legendre-Fenchel transform reduces to Legendre transform if the rate function is convex

$$\varphi_{\{\rho_i\}}(\{\lambda_i\}) = \sum_i \lambda_i \rho_i - \psi_{\{\rho_i\}}(\{\rho_i\}), \quad (\text{A.3})$$

where λ_i and ρ_i are one by one related via the stationary condition

$$\lambda_k = \frac{\partial \psi_{\{\rho_i\}}(\{\rho_i\})}{\partial \rho_k}, \quad \forall k \in \{1, \dots, N\}. \quad (\text{A.4})$$

Another consequence of the large-deviation principle is the so-called contraction principle. This principle suggests that when dealing with a set of random variables τ_i following a LDP and connected to ρ_i through the continuous mapping f , the rate function of ρ_i can be determined as follows

$$\psi_{\{\rho_i\}}(\{\rho_i\}) = \inf_{\{\tau_i\}: f(\{\tau_i\})=\{\rho_i\}} \psi_{\{\tau_i\}}(\{\tau_i\}). \quad (\text{A.5})$$

In more tangible terms, this statement suggests that an uncommon change in the behavior of ρ_i is predominantly influenced by the most probable variation among all unlikely changes in τ_i .

In the context of cosmology, if we take ρ_k to denote the late-time densities, then $\bar{\tau}_k$, the most likely initial field configuration, is obtained through the most probable mapping between the linear and late-time fields. In 2D, this most likely dynamics is given by cylindrical collapse, which is known to be well-fitted by

$$\zeta(\bar{\tau}_k) = \rho_k = \left(1 - \frac{\bar{\tau}_k}{\nu}\right)^{-\nu}. \quad (\text{A.6})$$

The choice of ν as 1.4 is made to match the calculated value of the third-order skewness of the matter density contrast in cylinders from perturbation theory, as presented in [Uhlemann et al. \(2018\)](#). The standard result for spherical collapse dynamics in 1 to 3D can be found in [Mukhanov \(2005\)](#).

Now that we know the most likely connection between initial conditions and the late-time field configuration, we can compute the rate function for the late-time density field. It is expressed as follows

$$\psi(\rho_i) = \frac{\sigma_{R_1}^2}{2} \sum_{k,j} \Xi_{k,j}(\tau_i) \bar{\tau}_k \bar{\tau}_j. \quad (\text{A.7})$$

Here, $\sigma_{R_1}^2$ is the driving parameter and is determined by the variance within the largest disk R_1 . $\Xi_{k,j}$ is the inverse covariance matrix between the linear density field inside the initial disks of radii $R_k \rho_k^{1/2}$.

Appendix A.2: Applying LDT to aperture mass PDF

Following [Barthelemy et al. \(2021\)](#), an accurate modelling of the top-hat smoothed weak lensing convergence can be obtained (Limber) approximating that the convergence field is an assembly of statistically independent infinitely long cylinders of the underlying matter density contrast. Those cylinders are centred on slices along the line of sight, and they reduce to those 2D slices as illustrated in [Fig. A.1](#). This means that the cumulants can be written as

$$\langle M_{ap}^p \rangle_c = \int_0^{\chi_s} d\chi \omega(\chi, \chi_s) \langle (\delta_{<\mathcal{D}(\chi)\theta_2} - \delta_{<\mathcal{D}(\chi)\theta_1})^p \rangle_c, \quad (\text{A.8})$$

where $\delta_{<\mathcal{D}(\chi)\theta_2} - \delta_{<\mathcal{D}(\chi)\theta_1}$ is a random variable that defines the slope between two concentric disks of radii $\mathcal{D}(\chi)\theta_2$ and $\mathcal{D}(\chi)\theta_1$

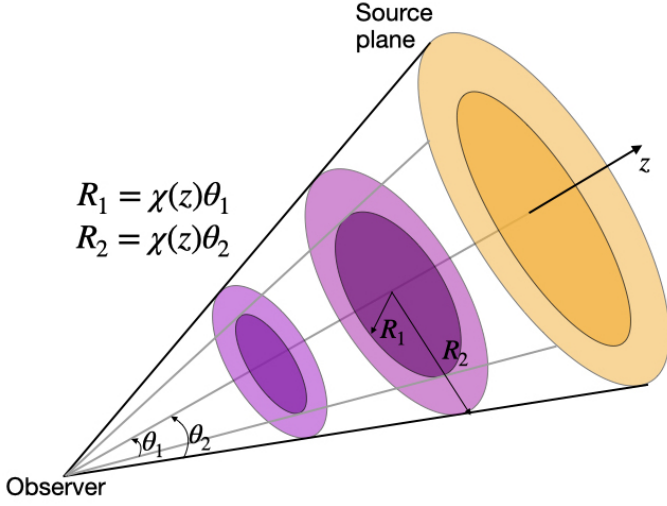


Fig. A.1. Schematic view of the procedure to obtain the aperture mass map following (Barthelemy et al. 2021). The projected quantities can be inferred as a superposition of the underlying 3D density field along the line of sight.

at comoving radial distance χ . This simplifies the problem greatly, now having to calculate just the one-point statistics related to the density slope within each two-dimensional slice along the line of sight.

As is explained in Appendix A of Barthelemy et al. (2021), the choice of driving parameter is not predicted by theory and is left as a free parameter. However, when computing the joint statistics of the density fields at different scales, this choice prevents us from imposing correct quadratic contributions in the CGF. This leads us to use the full non-linear prescription coming from the Halofit to model the non-linear covariance. In this paper, we use the Halofit-Takahashi version Takahashi et al. (2012) to compute the covariances.

Now using Eq. (A.3), and Eq. (A.7), and since we need the density slope between two concentric disks, we get the SCGF as

$$\varphi_{\delta_2-\delta_1}(\lambda) = \varphi_{\delta_1,\delta_2}(-\lambda, \lambda) \quad (\text{A.9})$$

To ensure that this choice does not lead to any discrepancies with the numerical simulations, we also rescale the projected CGF given in Eq. (A.3) with the measured variance $\sigma_{M_{ap},sim}^2$ instead of the one computed from Halofit $\sigma_{M_{ap},hfit}^2$ as is given below

$$\phi_{M_{ap}}(\lambda) = \frac{\sigma_{M_{ap},hfit}^2}{\sigma_{M_{ap},sim}^2} \phi_{M_{ap}} \left(\lambda \frac{\sigma_{M_{ap},sim}^2}{\sigma_{M_{ap},hfit}^2} \right) \quad (\text{A.10})$$

Once the CGF of individual slices is obtained, we can use Eq. (A.8) to get the CGF (the details of this derivation is given in Barthelemy et al. (2021)) of the lensing aperture mass as

$$\phi_{\kappa,\theta_1,\theta_2}(\lambda) = \int_0^{\chi_s} d\chi w^p(\chi, \chi_s) \phi_{\delta_1,\delta_2,M_{ap}}(w(\chi, \chi_s)\lambda, \mathcal{D}(\chi)\theta_1, \mathcal{D}(\chi)\theta_2). \quad (\text{A.11})$$

After calculating the CGF, the inverse Laplace transform can be used to obtain the convergence PDF

$$P(\kappa) = \int_{-i\infty}^{+i\infty} \frac{d\lambda}{2\pi i} \exp(-\lambda\kappa + \phi_{\kappa,\theta}(\lambda)). \quad (\text{A.12})$$

As described in more detail in Barthelemy et al. (2021), the inverse Laplace transform we need to perform assumes that the CGF is defined in the complex plane along the path of integration. Unfortunately, the use of numerical results for the matter power spectra prevents us to perform this continuation from the real axis. As a result, we use an informed fit of the numerical CGF along the real axis with a finite number of coefficients that we then extend to the complex plane. This allows to perform the previous integral.

Now that we have a PDF of the aperture mass map $P(M_{ap})$ / alternatively the wavelet coefficients, we could use that to obtain the wavelet ℓ_1 -norm using the Eq. (12) as demonstrated in the Sect. 3.3.